J|A|C|S

A R T I C L E S

Gas-Phase S$_N$2 and Bromine Abstraction Reactions of Chloride Ion with Bromomethane: Reaction Cross Sections and Energy Disposal into Products

Laurence A. Angel and Kent M. Ervin*

Contribution from the Department of Chemistry and Chemical Physics Program, University of Nevada, Reno, Nevada 89557

Received July 22, 2002; E-mail: ervin@chem.unr.edu

Abstract: Reaction cross sections and product velocity distributions are presented for the bimolecular gas-phase nucleophilic substitution (S$_N$2) reaction Cl$^-$ + CH$_3$Br → CH$_3$Cl + Br$^-$ as a function of collision energy, 0.06−24 eV. The exothermic S$_N$2 reaction is inefficient compared with phase space theory (PST) and ion−dipole capture models. At the lowest energies, the S$_N$2 reaction exhibits the largest cross sections and symmetrical forward/backward scattering of the CH$_3$Cl + Br$^-$ products. The velocity distributions of the CH$_3$Cl + Br$^-$ products are in agreement with an isotropic PST distribution, consistent with a complex-mediated reaction and a statistical internal energy distribution of the products. Above 0.2 eV, the velocity distributions become nonisotropic and nonstatistical, exhibiting CH$_3$Cl forward scattering between 0.2 and 0.6 eV. A rebound mechanism with backward scattering above 0.6 eV is accompanied by a new rising feature in the CH$_3$Cl + Br$^-$ cross sections. The competitive endothermic reaction Cl$^-$ + CH$_3$Br → CH$_3$ + ClBr$^-$ rises from its thermochemical threshold at 1.9 ± 0.4 eV, showing nearly symmetrically scattered products just above threshold and strong backward scattering above 3 eV associated with a second feature in the cross section.

Bimolecular nucleophilic substitution (S$_N$2) with inversion of the carbon center is a fundamental reaction mechanism in chemistry. Study of S$_N$2 reactions in the gas phase[1−5] allows examination of the intrinsic reaction mechanism in isolation from solvent. Laerdahl and Uggerud[1] have reviewed recent literature in the area. The most extensively studied gas-phase S$_N$2 reaction is of a halide ion with halomethane, reaction 1,

$$X^- + CH_3Y \rightarrow XCH_3 + Y^- \qquad (1)$$
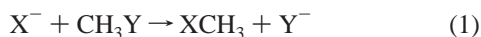
which proceeds through a double-well potential energy surface (PES).[6−8] Two potential energy minima correspond to ion−molecule intermediates on both the reactant and product sides of a central energy barrier, corresponding to the pentacoordinate [X−CH$_3$−Y]$^-$ transition state. A schematic PES exhibiting the C_{3v} stationary points for reaction 2 is shown in Figure 1.

$$Cl^- + CH_3Br \rightarrow ClCH_3 + Br^- \qquad (2)$$

Exothermic S$_N$2 reactions of halide ions with halomethanes proceed below the collision rate of the reactants,[6,9−13] even in cases such as reaction 2 where the central barrier lies below

the energy of the reactants. Reaction inefficiency results from dynamical constraints accompanying the PES central barrier.[4,14−17,18−21] Four possible dynamical bottlenecks that have been identified are angular momentum constraints, inefficient energy transfer among modes, mode-specific energy requirements, and steric factors. Kinetic energy and random impact parameters in the initial collision results in orbital angular momentum, which leads to centrifugal barriers.[14,17,22−25] Formation of the entrance channel complex may be restricted by poor

(1) Laerdahl, J. K.; Uggerud, E. *Int. J. Mass Spectrom.* **2002**, *214*, 277−314.
(2) Gronert, S. *Chem. Rev.* **2001**, *101*, 329−360.
(3) Chabinyc, M. L.; Craig, S. L.; Regan, C. K.; Brauman, J. I. *Science* **1998**, *279*, 1882−1886.
(4) Hase, W. L. *Science* **1994**, *266*, 998−1002.
(5) Shaik, S. S.; Schlegel, H. B.; Wolfe, S. *Theoretical Aspects of Physical Organic Chemistry: The S$_N$2 Mechanism*; John Wiley and Sons: New York, 1992.
(6) Olmstead, W. N.; Brauman, J. I. *J. Am. Chem. Soc.* **1977**, *99*, 4219−4228.
(7) Dodd, J. A.; Brauman, J. I. *J. Phys. Chem.* **1986**, *90*, 3559−3562.

(8) Brauman, J. I. *J. Mass Spectrom.* **1995**, *30*, 1649−1650.
(9) DePuy, C. H.; Gronert, S.; Mullin, A.; Bierbaum, V. M. *J. Am. Chem. Soc.* **112**, *112*, 8650−8655.
(10) O'Hair, R. A.; Davico, G. E.; Hacaloglu, J.; Dang, T. T.; DePuy, C. H.; Bierbaum, V. M. *J. Am. Chem. Soc.* **1994**, *116*, 3609−3610.
(11) Angel, L.; Ervin, K. *J. Phys. Chem. A* **2001**, *105*, 4042−4051.
(12) Le Garrec, J.-L.; Rowe, B. R.; Queffelec, J. L.; Mitchell, J. B. A.; Clary, D. C. *J. Chem. Phys.* **1997**, *107*, 1021−1024.
(13) Kato, S.; Davico, G. E.; Lee, H. S.; Depuy, C. H.; Bierbaum, V. M. *Int. J. Mass Spectrom.* **2001**, *210/211*, 223−229.
(14) Levine, R. D.; Bernstein, R. B. *J. Phys. Chem.* **1988**, *92*, 6954−6958.
(15) Wang, H.; Peslherbe, G. H.; Hase, W. L. *J. Am. Chem. Soc.* **1994**, *116*, 9644−9651.
(16) Peslherbe, G. H.; Wang, H.; Hase, W. L. *J. Am. Chem. Soc.* **1996**, *118*, 2257−2266.
(17) Wang, H.; Hase, W. L. *J. Am. Chem. Soc.* **1997**, *119*, 3093−3102.
(18) Su, T.; Wang, H.; Hase, W. L. *J. Phys. Chem. A* **1998**, *102*, 9819−9828.
(19) Su, T.; Morris, R. A.; Viggiano, A. A.; Paulson, J. F. *J. Phys. Chem.* **1990**, *94*, 8426−8430.
(20) Schmatz, S.; Clary, D. C. *J. Chem. Phys.* **1999**, *110*, 9483−9491.
(21) Schmatz, S. *Chem. Phys. Lett.* **2000**, *330*, 188−194.
(22) Levine, R. D.; Bernstein, R. B. *Molecular Reaction Dynamics and Chemical Reactivity*; Oxford University Press: New York, 1987.
(23) Mann, D. J.; Hase, W. L. *J. Phys. Chem. A* **1998**, *102*, 6208−6214.
(24) DeTuri, V. F.; Hintz, P. A.; Ervin, K. M. *J. Phys. Chem. A* **1997**, *101*, 5969−5986.
(25) Angel, L. A.; Garcia, S. P.; Ervin, K. M. *J. Am. Chem. Soc.* **2002**, *124*, 335−345.
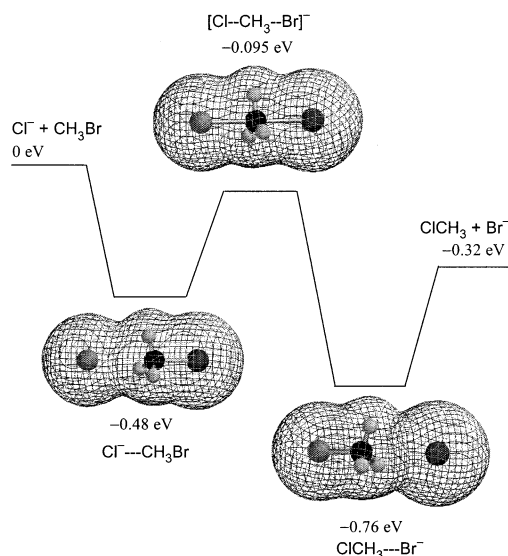
Figure 1. Schematic potential energy surface for reaction 2 in C_{3v} symmetry. The energies of the stationary points relative to reactants are calculated by Schmatz et al.[50] at the CCSD(T)/431cGTOs level and corrected for basis set superposition error and zero-point energy. The diagrams of the stationary points illustrate the total electron density calculated at the SVWN/DN** level at the geometries calculated by Schmatz.

Table 1. Enthalpies of Reaction for $Cl^- + CH_3Br \rightarrow$ Products

reaction	products	ΔH_0 (exptl),[a] kJ mol^{-1}
	$Cl^- + CH_3Br$	0
2	$Br^- + CH_3Cl$	-31 ± 1
3	$ClBr^- + CH_3$	184 ± 14[b]
	$CH_2Br^- + HCl$	248 ± 12[c]
	$CH_2Cl^- + HBr$	264 ± 18[d]
	$Cl^- + CH_3 + Br$	289 ± 1
	$Br^- + CH_3 + Cl$	313 ± 1
	$Br^- + HCl + CH_2$	341 ± 4
	$Br^- + CH_2Cl + H$	379 ± 10
	$Cl^- + HBr + CH_2$	383 ± 4
	$Cl^- + CH_2Br + H$	403 ± 14[e]
	$CHCl^- + H_2 + Br$	487 ± 30[f]
	$CHBr^- + H_2 + Cl$	601 ± 17[g]
	$CHBr^- + HCl + H$	605 ± 17[g]
	$CH_2Cl^- + H + Br$	627 ± 18[d]
	$ClBr^- + CH + H_2$	628 ± 14[b]
	$CHCl^- + HBr + H$	629 ± 30[f]
	$CBr^- + HCl + H_2$	630 ± 35[h]
	$ClBr^- + CH_2 + H$	640 ± 17[b]
	$CCl^- + HBr + H_2$	660 ± 40[h]
	$CH_2Br^- + H + Cl$	676 ± 12[c]
	$CHCl^- + H + H + Br$	919 ± 30[f]
	$CHBr^- + H + H + Cl$	1033 ± 17[g]

[a] Enthalpies of reactions calculated with enthalpies of formation values cited in Gurvich et al.[69,70] except as noted. [b] Using EA(ClBr) = 2.47 $\pm$ 0.13 eV calculated here at the CCSD(T)/aug-cc-pVTZ level. [c] Calculated using $\Delta_f H_0(CH_2Br^-) = 90 \pm 12$ kJ/mol.[73,74] [d] Calculated using EA(CH$_2$Cl) = 0.80 $\pm$ 0.16 eV determined by Bartmess[72] from work by Ingemann and Nibbering.[71] [e] Calculated using EA(CH$_2$Br) = 0.79 $\pm$ 0.14 eV determined by Bartmess[72] from work by Hierl et al.[74] [f] Calculated using EA(CHCl) = 1.210 $\pm$ 0.005 eV published by Gilles et al.[76] [g] Calculated using $\Delta_f H_0(CHBr^-) = 231 \pm 17$ kJ/mol determined by Bartmess[72] from work by Gilles et al.[76] and Ingemann and Nibbering.[75] [h] Using EA(CCl) = -0.024 eV and EA(CBr) = 0.23 eV calculated here at the CCSD(T)/aug-cc-pVTZ level.

energy coupling between "intermolecular" modes of the $Cl^-\cdots CH_3Br$ ion$-$dipole complex (the stretch and two bending modes of $Cl^-\cdots CH_3Br$) and "intramolecular" CH_3Br modes (the vibrations of CH_3Br), resulting in a high dissociation rate back to reactants.[4,26$-$28] Crossing of the PES central barrier has been shown to be sensitive to mode-specific internal energy distributions.[4,15,16,25,29$-$31] The highly structured nature of the S_N2 transition state restricts the orientation of the reactants to lie nearly along the C_{3v} axis of CH_3Y.

Influence from dynamical constraints has brought into question the validity of statistical theories such as Rice$-$Ramsperger$-$Kassel$-$Marcus (RRKM) theory and phase space theory (PST) in modeling reaction 1. Several studies[4,13,15,16,27,28,31$-$35] on reaction 2 in particular have suggested that the reaction behaves nonstatistically. Graul and Bowers[32,33] determined that the dissociation of metastable $Cl^-\cdots CH_3Br$ complex ions results in translationally cold Br^- + CH_3Cl products, as compared with the prediction of PST, coincident with high internal excitation of CH_3Cl. The rate coefficients for reaction 2 have been found by Viggiano and co-workers to be independent of the internal temperature of CH_3-Br at fixed kinetic energies,[34] which is not consistent with RRKM theory for reaction 2.[35] Classical trajectory calculations by Hase and co-workers[4,15,16,28,36] have found nonstatistical and

non-RRKM behavior such as inefficient mode coupling, central barrier recrossing, and a direct S_N2 reaction mechanism. Tonner and McMahon[31] observed that formation of the CH_3Cl + Br^- products is enhanced by mode-specific vibrational excitation of C$-$Br in the $Cl^-\cdots CH_3Br$ complex. The observed deuterium kinetic isotope effect is inverse ($k_D > k_H$) as predicted by transition state theory, but experimentally the isotope effect is significantly stronger than predicted statistically.[13,35,37]

A basic tenet of statistical rate theory is that internal energy is randomized among all available modes and only the total energy, angular momentum, and densities of states determine the dissociation rate into products.[4,38] Statistical transition state theory models such as PST can account for angular momentum conservation (one possible dynamic restriction on reaction 2) but not for nonstatistical behavior such as steric factors, poor energy transfer, or mode-specific reactivity. Recrossings of the dividing surface at the transition state, identified in trajectory calculations for reaction 2,[15] represent a violation of an additional fundamental assumption of statistical rate theory.

In addition to the S_N2 products, reaction 2, we observe endothermic Br abstraction, reaction 3, which is driven by translational energy in the collision energy range 1.9$-$20 eV.

$$Cl^- + CH_3Br \rightarrow CH_3 + ClBr^- \qquad (3)$$
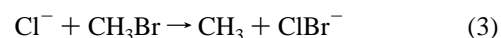
The reaction energetics are given in Table 1. Reaction 3 has been previously reported by Cyr et al.[39] Competition between

(26) Cho, Y. J.; Vande Linde, S. R.; Zhu, L.; Hase, W. L. *J. Chem. Phys.* **1992**, *96*, 8275$-$8287.
(27) Wang, H.; Hase, W. L. *Chem. Phys.* **1996**, *212*, 247$-$258.
(28) Wang, H.; Goldfield, E. M.; Hase, W. L. *J. Chem. Soc., Faraday Trans.* **1997**, *93*, 737$-$746.
(29) Vande Linde, S. R.; Hase, W. L. *J. Am. Chem. Soc.* **1989**, *111*, 2349$-$2351.
(30) Ayotte, P.; Kim, J.; Kelley, J. A.; Nielsen, S. B.; Johnson, M. A. *J. Am. Chem. Soc.* **1999**, *121*, 6950$-$6951.
(31) Tonner, D. S.; McMahon, T. B. *J. Am. Chem. Soc.* **2000**, *122*, 8783$-$8784.
(32) Graul, S. T.; Bowers, M. T. *J. Am. Chem. Soc.* **1991**, *113*, 9696$-$9697.
(33) Graul, S. T.; Bowers, M. T. *J. Am. Chem. Soc.* **1994**, *116*, 3875$-$3883.
(34) Viggiano, A. A.; Morris, R. A.; Paschkewitz, J. S.; Paulson, J. F. *J. Am. Chem. Soc.* **1992**, *114*, 10 477$-$10 482.
(35) Wang, H.; Hase, W. L. *J. Am. Chem. Soc.* **1995**, *117*, 9347$-$9356.
(36) Wang, Y.; Hase, W. L. *J. Chem. Phys.*, in press.

(37) Hu, W.-P.; Truhlar, D. G. *J. Am. Chem. Soc.* **1995**, *117*, 10 726$-$10 734.
(38) Baer, T.; Hase, W. L. *Unimolecular Reaction Dynamics: Theory and Experiments*; Oxford University Press: New York, 1996.

halogen abstraction reactions and S_N2 has also been observed previously in our laboratory, including Cl_2^- from the reaction $Cl^- + CH_3Cl$[24] and FCl^- from $F^- + CH_3Cl$ and $Cl^- + CH_3F$.[11,25]

The S_N2 and Br abstraction reactions may be categorized as proceeding by either a backside or front-side attack mechanism. The S_N2 PES shown in Figure 1 illustrates the backside attack where the path of the approaching Cl^- lies on the methyl side of CH_3Br. Front-side attack is where the Cl^- approaches the CH_3Br molecule from the C—Br bond side and may result in Br^- displacement or Br abstraction at higher energies. The competing reactions may also be characterized as proceeding via a complex-mediated or a direct reaction mechanism. Complex-mediated reactions are usually expected to result in isotropic scattering and statistical energy distributions of the products. A direct mechanism, in contrast, involves an impulsive collision, resulting in anisotropic scattering and nonstatistical energies of the products. Intermediate cases are also possible.

This paper presents the cross sections for reactions 2 and 3 for the center-of-mass collision energy range 0.06−24 eV. The velocity distributions of the products are also measured, revealing information on the reaction mechanism and the distribution of available energy into kinetic and internal energy. Phase space theory and ab initio calculations are used to help interpret the experimental results.

Experimental Methods

Our guided ion beam (GIB) mass spectrometer has been recently modified with two sequential octopole ion guide regions replacing the original single octopole. This split octopole arrangement provides for time-of-flight (TOF) measurements used in determining the velocity distributions of reaction products. The original configuration has been described in detail.[24] A brief description is presented here with emphasis on the recent modifications.

Chloride anions are produced in a microwave discharge source from room-temperature trichloromethane, $CHCl_3$, introduced into a flowing He buffer gas. The ions pass along a flow tube and are sampled through a nose cone. The Cl^- ion beam is then shaped, focused, and accelerated by a series of lenses to a magnetic mass spectrometer, which mass selects the $^{35}Cl^-$ ions. A bipolar deflector after the second slit of the magnetic sector is used to pulse the ion beam when required. Another set of lenses guides the $^{35}Cl^-$ ion beam into the first radio frequency octopole ion trap. The radio frequency potentials are applied to the octopoles by a radio frequency power source,[40] with a frequency of 4.4 MHz and amplitude of 60 V for the present work. The length of the first octopole is 33.5 cm. Situated at the center of the first octopole is a reaction cell (3.2-cm long body with two 3.5-cm extension tubes), where the bromomethane (Matheson Tri-Gas, 99%) reactant gas is introduced. The effective path length of the reaction cell is 7.0 cm based on calibrations against the previous gas cell configuration (8.9-cm body with 5.7-cm extensions), for which an effective path length of 14.6 cm was estimated.[24] The collision energy between the chloride ions and the neutral bromomethane is controlled by the dc potential difference between the flow tube ion source and the first octopole. The anionic reactants and products are collected and guided by the second octopole (length = 67.8 cm), which is floated at a dc voltage offset above the first octopole, to a quadrupole mass spectrometer where they are mass analyzed. Ion intensities are detected by a collision dynode/channeltron multiplier operated in negative-ion pulse counting mode.

Possible light product species (e^- and H^-) are not detected because of inefficient trapping by the octopole beam guide and the lower mass limit of the quadrupole mass spectrometer.

Absolute reaction cross sections are determined as a function of collision energy by scanning the octopole dc potential and counting the reactant and product ions for predetermined dwell times.[24] The laboratory ion energy is measured by using retarding potential analysis, confirmed by time-of-flight measurements, and converted to relative collision energy, E, in the center-of-mass (c.m.) frame.[24,41] Background ion counts occurring outside the reaction cell are also collected and subtracted from the total. All cross sections are measured at three pressures in the range $(1−5) \times 10^{-5}$ mbar. The results are extrapolated to zero pressure by a least-squares linear regression, ensuring that the reported cross sections are in the single-collision limit.[24,41] The threshold behavior of the $ClBr^-$ cross section is modeled using an empirical threshold law described previously,[24,41−44] using the CRUNCH program.[45] Reported error limits for fits to cross sections are propagated from individual known sources of uncertainty and represent ± 2 combined standard uncertainties[46] or an approximate 95% confidence level. The estimated accuracy of absolute cross section magnitudes is $\pm 50\%$ and is limited by the determination of the effective gas cell length and the cell pressure.

Reactant and product ion axial velocity distributions are recorded by using the octopoles as the free flight region for TOF measurements, using methods that have been previously developed by several groups.[47−49] A pulsed Cl^- ion beam is prepared by applying a pair of bipolar symmetrical voltage pulses on the deflectors with pulse widths in the range of $10−150$ μs. The ion TOFs are measured by using a multichannel scalar (EG&G TurboMCS) triggered by the deflector pulse. The recorded Cl^- TOF is converted to axial velocity distributions by inversion of eq 4.[49]

$$t_i = t_0 + \frac{l_1}{v_i} + \frac{l_2}{(v_i^2 + 2q\Delta V/m_i)^{1/2}} \tag{4}$$

The first term t_0 represents the TOF outside the two octopoles. The second and third terms represent the TOF spent inside the two octopoles, where l_1 and l_2 are the lengths of the first and second octopole, respectively. Indices i refer to Cl^- reactant ions, t_i is the total TOF measured, v refers to axial laboratory velocity in the first octopole, q and m are the charge and mass of ions, and ΔV is the dc offset between the first and second octopole. The TOF spectra for the product ions, Br^- or $ClBr^-$, are converted to axial velocities via eq 5.

$$t_p = t_1 + \frac{l_1}{2\langle v_i \rangle} + \frac{l_1}{2v_p} + \frac{l_2}{(v_p^2 + 2q\Delta V/m_p)^{1/2}} + t_5\left(\frac{m_p}{m_i}\right)^{1/2} \tag{5}$$

The first term t_1 is the Cl^- TOF from the pulsing lens to the first octopole. The second term represents the Cl^- TOF from the beginning of the first octopole to the reaction cell, where $\langle v_i \rangle$ is the average laboratory velocity of Cl^-. The third and fourth terms are the product ion TOFs from the reaction cell to the end of the second octopole, where indices p refer to the product ion, and the final term is the TOF

(39) Cyr, D. A.; Scarton, M. G.; Wiberg, K. B.; Johnson, M. A.; Nonose, S.; Hirokawa, J.; Tanaka, H.; Kondow, T.; Morris, R. A.; Viggiano, A. A. *J. Am. Chem. Soc.* **1995**, *117*, 1828−1832.
(40) Jones, R. M.; Gerlich, D.; Anderson, S. L. *Rev. Sci. Instrum.* **1997**, *68*, 3357−3362.

(41) Ervin, K. M.; Armentrout, P. B. *J. Chem. Phys.* **1985**, *83*, 166−189.
(42) Armentrout, P. B. *Int. J. Mass Spectrom.* **2000**, *200*, 219−241.
(43) Schultz, R. H.; Crellin, K. C.; Armentrout, P. B. *J. Am. Chem. Soc.* **1991**, *113*, 8590−8601.
(44) Dalleska, N. F.; Honma, K.; Sunderlin, L. S.; Armentrout, P. B. *J. Am. Chem. Soc.* **1994**, *116*, 3519−3528.
(45) Armentrout, P. B.; Ervin, K. M. *CRUNCH*; Fortran program, version 5.0, 2002.
(46) Taylor, B. N.; Kuyatt, C. *Guidelines for Evaluating and Expressing the Uncertainty of NIST Measurement Results*; NIST Technical Note 1297; Washington, DC: National Institute of Standards and Technology, 1994. http://physics.nist.gov/Document/tn1297.pdf.
(47) Gerlich, D. *Adv. Chem. Phys.* **1992**, *82*, 1−176.
(48) Dressler, R. A.; Salter, R. H.; Murad, E. *Chem. Phys. Lett.* **1993**, *204*, 111−118.
(49) Muntean, F.; Armentrout, P. B. *J. Chem. Phys.* **2001**, *115*, 1213−1228.

through the quadrupole mass spectrometer detector. The total dead time for reaction ions, t_0, is the sum of t_1 and t_5. A calibration procedure is performed to determine t_0. TOF spectra are recorded at a series of octopole dc voltages. The TOF peaks are fit to eq 6 where V_0 represents the potential of the ion source.

$$t_i = t_0 + \frac{l_2}{(2q_i(V - V_0)/m_i)^{1/2}} + \frac{l_2}{(2q_i(V + \Delta V - V_0)/m_i)^{1/2}} \quad (6)$$

A nonlinear least-squares fit of eq 6 is used to determine initial values for t_0 and V_0. The TOF measurement for V_0 is then compared to the V_0 value obtained by retarding potential measurements.[24] The agreement is typically within 0.05 eV at energies below 1 eV and within 0.2 eV at higher energies. These discrepancies are systematic and, as discussed previously, can be attributed to the effect on the TOFs of variable field penetration by the entrance and exit lenses before and after the octopoles as the octopole dc voltage is changed.[24] The V_0 value obtained by the retarding potential analysis is therefore used in eq 6 to calculate the final t_0 value. We find that t_0 can be accurately calculated by using the known lengths and potentials of ion lenses along the beam line, and therefore estimates of its division into t_1 and t_5 for eq 5 are made by using similar calculations. All time-to-velocity conversions include the appropriate Jacobian transforms of the intensities on the basis of eqs 4 and 5.

The measured velocity distributions represent the components of the three-dimensional scattering vectors projected along the ion beam axis. Conversion of axial velocity distributions from the laboratory to the center-of-mass frame is given by eqs 7 and 8, which assume a stationary CH_3Br target,[22,49]

$$u_p = v_p - v_{cm} \quad (7)$$

$$v_{cm} = m_i v_p / m_{total} \quad (8)$$

where v represents laboratory velocities and u represents velocities in the center-of-mass (c.m.) frame, v_{cm} is the laboratory velocity of the center-of-mass of the system, v_i is the laboratory ion velocity before collision, and m_{total} is the total mass. Individual product velocities in the center-of-mass frame are then converted to relative product velocities for reactions 2 and 3 by eqs 9 and 10.

$$u_{rel} = u_{CH_3Cl} - u_{Br^-} = -\frac{m_{total}}{m_{CH_3Cl}} u_{Br^-} \quad \text{(reaction 2)} \quad (9)$$

$$u_{rel} = u_{BrCl^-} - u_{CH_3} = \frac{m_{total}}{m_{CH_3}} u_{BrCl^-} \quad \text{(reaction 3)} \quad (10)$$

These equations describe the directional scattering of the product species containing the Cl atom for positive values of u_{rel}.

At collision energies below 0.6 eV, the Br^- product TOF spectra exhibit a pressure-dependent artifact, observed as a tail at long times as shown in Figure 2a for 0.10 eV. This phenomenon is due to ions that undergo a velocity-slowing collision and then become trapped by the octopole rf potentials.[24] These trapped ions eventually undergo additional collisions, react, and drift to the detector. To eliminate the artifactual signal, two procedures are combined. First, the lowest CH_3Br gas cell pressure of 0.02 μbar is used, reducing the artifact to a minimum. Second, the radio frequency trapping field applied to the octopoles is switched off after a delay that allows the majority of the Br^- ion signal to be collected. The rf remains off for a 20–50-μs period, long enough to eliminate the trapped ions from the octopoles before the next pulse cycle. Figure 2a shows that the procedure allows for the main feature of the Br^- signal to be collected, and Figure 2b shows the resulting product relative velocity distribution. However, eliminating trapped ions does result in a loss of the most-backward-scattered Br^- products in the lab frame. Therefore the product velocity distributions,
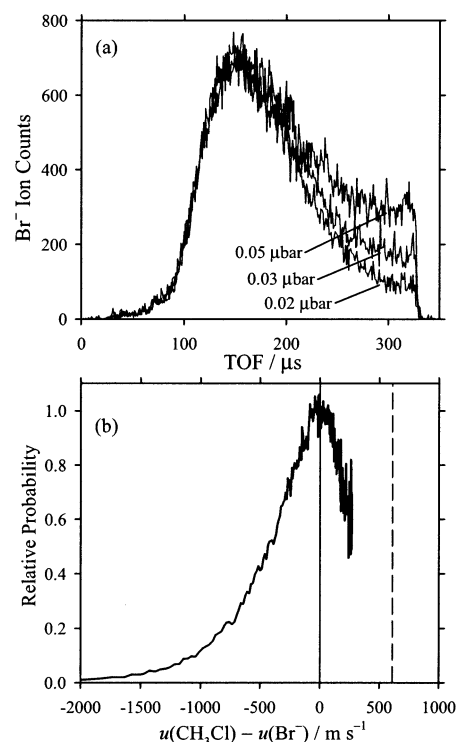
Figure 2. (a) The Br^- time-of-flight spectrum at 0.10 eV c.m. and three CH_3Br gas cell pressures of 0.05, 0.03, and 0.02 μbar. The artifactual signal above 200 μs decreases as the gas cell pressure is reduced. (b) Transform of the time-of-flight spectrum at 0.02 μbar to the product axial relative velocity distribution in the center-of-mass frame. The solid vertical line is the zero center-of-mass velocity; the dashed vertical line is the relative velocity above which the Br^- ions would be backward scattered in the lab frame.

for low collision energies, are truncated for positive values of u_{rel} from eq 9 (corresponding to the most-forward-scattered CH_3Cl products in the c.m. frame). The time-to-velocity transformation compresses the long-time portion of the spectrum corresponding to positive values of u_{rel} in Figure 2b. Measurement of the product velocities for collision energies below 0.10 eV c.m. (0.14 eV lab) were not feasible because of this effect and because of the ion energy spread (typically 0.26 eV lab full width at half-maximum). The integral cross-section measurements also employ a pulsed mode of operation to eliminate the effect of ions that are trapped for long times, as described previously,[24] but with a longer delay of about 1 ms before the rf is switched off to collect all product ions that have a forward laboratory velocity component.

The potential offset of the second octopole, ΔV in eq 4, would normally be set to a value a few volts higher than the first octopole, high enough to efficiently extract ions from the first octopole but still low for good dispersion of the times-of-flight for different product velocities.[48,49] However, for reaction 2 the high cross section at low energies results in a significant background signal from residual CH_3Br in the second octopole region. Therefore, the ion energy in the second octopole is set above 100 eV, where the reaction cross section is small. There is still sufficient time resolution as shown in Figure 2.

Theoretical Methods

Reaction 2 has been studied extensively by ab initio methods.[1] Most theoretical values needed for statistical reaction models here are taken from recent high level coupled cluster CCSD(T) calculations by Schmatz et al.[50] Other calculations needed for modeling parameters or interpretation were performed by

(50) Schmatz, S.; Botschwina, P.; Stoll, H. *Int. J. Mass Spectrom.* **2000**, *201*, 277–282.

Table 2. Molecular Parameters Used in the PST Model

	$Cl^- + CH_3Br$	$Cl^-(CH_3Br)$	$[Cl-CH_3-Br]^-$	$ClBr^- + CH_3$	$Br^- + CH_3Cl$
vibrational frequencies,[a] cm^{-1}	3197 (64) [2]	3247 (65) [2]	3397 (68) [2]	3291 (66) [2]	3184 (64) [2]
	3087 (62)	3125 (63)	3178 (64)	3102 (62)	3080 (62)
	1492 (15) [2]	1476 (15) [2]	1420 (14) [2]	1406 (14) [2]	1501 (15) [2]
	1339 (13)	1276 (13)	1020 (10)	498 (6)	1386 (14)
	972 (10) [2]	932 (9) [2]	972 (10) [2]	203 (1.2)[f]	1034 (10) [2]
	622 (3)	531 (3)	186 (1)		741 (4)
		102 (0.7)[f]	185 (1) [2]		
		76 (0.4)[f] [2]			
rotational constants,[b] cm^{-1}	5.222	5.238	4.853	9.325	5.251
	0.318	0.027	0.030	9.325	0.443
	0.318	0.027	0.030	4.663	0.443
				0.090	
polarizability,[c] Å^3	5.87			1.93	5.35
dipole moment,[d] debye	1.81				1.87
rotational symmetry	3	3	3	6	3
E_0,[e] eV	0.0	−0.48	−0.095	1.91[g]	−0.32

[a] CCSD(T) harmonic frequencies from Schmatz et al.,[50] except CH_3 and $ClBr^-$ calculated here at the CCSD(T)/aug-cc-pVDZ level. Estimated[61] anharmonicity constants given in parentheses. Degeneracies given in brackets. [b] Rotational constants calculated by using CCSD(T) geometries from Schmatz et al.,[50] except CH_3 and $ClBr^-$ calculated here at the CCSD(T)/aug-cc-pVDZ level. [c] Miller.[59] [d] Nelson et al.[60] [e] CCSD(T) energy relative to reactants including counterpoise correction from Schmatz et al.[50] and corrected for zero point energy using the anharmonic frequencies. [f] Anharmonicity based on Morse potential and dissociation energy. [g] From Table 1.

standard methods. Møller−Plesset (MP2) and coupled cluster (CCSD(T)) calculations were performed by using Gaussian 98.[51] A S_N2 pseudocollinear potential energy surface was calculated at the MP2/aug-cc-pVDZ //MP2/CEP-121G level, selected for speed and reasonable relative energies of stationary points.[52] Front-side attack stationary points and one-dimensional cuts through the potential energy surface were calculated by using MP2/aug-cc-pVDZ. The electron affinities of the dihalogens were calculated at the CCSD(T)/aug-cc-pVTZ level. Rotational constants and vibrational frequencies for the $ClBr^- + CH_3$ channel were calculated at the CCSD(T)/aug-cc-pVDZ level. Spartan[53] was used for illustrating the total electron densities at stationary points, as in Figure 1.

Phase space theory (PST), a form of transition state theory that explicitly conserves angular momentum,[54] is used to model energy-dependent reaction cross sections or rates and product energy distributions. In the microcanonical PST model used here,[55−58] the total angular momentum is approximated by the orbital angular momentum from the collision process and the phase space for the rotational degrees of freedom of the transition states are calculated classically by using the spherical rotor approximation for nonlinear molecules. The $Cl^-\cdots CH_3Br$ ion−molecule complex is formed by capture over the centrifugal barrier of the long-range electrostatic ion−molecule potential,

followed by the statistical unimolecular decomposition of the complex either back to reactants via an orbiting transition state or to the $Br^- + CH_3Cl$ products via the fixed, tight S_N2 transition state barrier. A statistical distribution is assumed at the transition state with conservation of orbital angular momentum out to products. The competition from reaction 3 has also been included in the PST model, with products treated by an orbiting transition state. The molecular parameters are taken from experiments and theoretical calculations[50,59,60] and are presented in Table 2. Vibrational anharmonicities are estimated as described by Duncan et al.[61] The sums and densities of states are calculated in the rigid-rotor Morse-oscillator approximation using the Beyer−Swinehart Stein−Rabinovitch direct count algorithm.[62−64] The PST cross sections are convoluted over the experimental kinetic energy distributions and the internal energy distribution of CH_3Cl at 300 K by numerical integration using the CRUNCH program.[45] Test calculations including the ion− dipole association complex by unified transition state theory[65] yielded no change in the calculated cross sections. Using either an ion-induced-dipole potential with zero permanent dipole for calculating the centrifugal barrier in the entrance channel or a locked-dipole approximation also makes no difference for the S_N2 product channel, because the reaction cross section is limited by the effective potential at the central barrier. Increasing the initial collision-capture probability in the PST model merely increases the probability for back-dissociation to reactants.

For modeling product energy distributions with phase space theory, we use a Fortran program obtained from the Michael T. Bowers group (University of California, Santa Barbara)[32,33,56,66] and modified to generate the axial relative velocity distributions assuming isotropic scattering of products in the

(51) Frisch, M. J.; Trucks, G. W.; Schlegel, H. B.; Scuseria, G. E.; Robb, M. A.; Cheeseman, J. R.; Zakrzewski, V. G.; Montgomery, J. A., Jr.; Stratmann, R. E.; Burant, J. C.; Dapprich, S.; Millam, J. M.; Daniels, A. D.; Kudin, K. N.; Strain, M. C.; Farkas, O.; Tomasi, J.; Barone, V.; Cossi, M.; Cammi, R.; Mennucci, B.; Pomelli, C.; Adamo, C.; Clifford, S.; Ochterski, J.; Petersson, G. A.; Ayala, P. Y.; Cui, Q.; Morokuma, K.; Malick, D. K.; Rabuck, A. D.; Raghavachari, K.; Foresman, J. B.; Cioslowski, J.; Ortiz, J. V.; Baboul, A. G.; Stefanov, B. B.; Liu, G.; Liashenko, A.; Piskorz, P.; Komaromi, I.; Gomperts, R.; Martin, R. L.; Fox, D. J.; Keith, T.; Al-Laham, M. A.; Peng, C. Y.; Nanayakkara, A.; Gonzalez, C.; Challacombe, M.; Gill, P. M. W.; Johnson, B.; Chen, W.; Wong, M. W.; Andres, J. L.; Gonzalez, C.; Head-Gordon, M.; Replogle, E. S.; Pople, J. A. *Gaussian98*; Revision A.7; Pittsburgh, PA: Gaussian, Inc., 1998.
(52) Hoyt, B.; Ervin, K. M., unpublished results.
(53) Deppmeier, B.; Driessen, A.; Hehre, T.; Hehre, W.; Johnson, J.; Klunzinger, P.; Lou, L.; Yu, J. *Spartan*; Wave function Inc.: Irvine, CA 92612.
(54) Pechukas, P.; Light, J. C. *J. Chem. Phys.* **1965**, *42*, 3281−3291.
(55) Chesnavich, W. J.; Bowers, M. T. *J. Chem. Phys.* **1977**, *66*, 2306−2315.
(56) Chesnavich, W. J.; Bowers, M. T. Statistical Methods in Reation Dynamics, In *Gas-Phase Ion Chemistry*; Michael T. Bowers, Ed.; Academic: New York, 1979; pp 119−151.
(57) Webb, D. A.; Chesnavich, W. J. *J. Phys. Chem.* **1983**, *87*, 3791−3798.
(58) Grice, M. E.; Song, K.; Chesnavich, W. J. *J. Phys. Chem.* **1986**, *90*, 3503−3509.

(59) Miller, T. M. Atomic and Molecular Polarizabilities, In *Handbook of Chemistry and Physics*, 71st ed.; Lide, D. R., Ed.; CRC Press: Boca Raton, FL, 1990; pp 10-193−10-209.
(60) Nelson, R. D.; Lide, D. R., Jr.; Maryott, A. A. Selected Values of Electric Dipole Moments in the Gas Phase. In *Handbook of Chemistry and Physics*; Lide, D. R., Ed.; CRC Press: Boca Raton, Florida, 1990; pp 9-6−9-8.
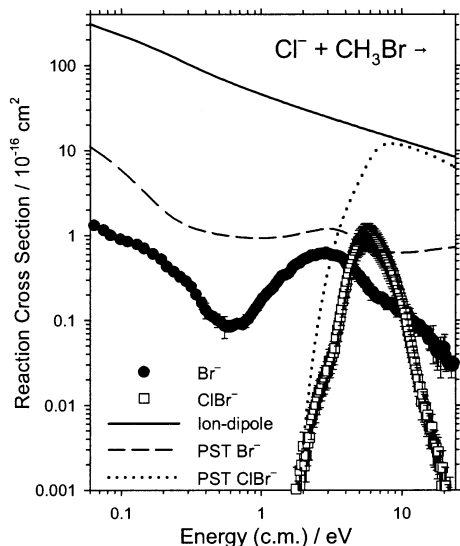(61) Duncan, J.; Allan, A. L.; McKean, D. C. *Mol. Phys.* **1970**, *18*, 289−303.
(62) Beyer, T. S.; Swinehart, D. F. *Commun. ACM* **1973**, *16*, 379.
(63) Stein, S. E.; Rabinovitch, B. S. *J. Chem. Phys.* **1973**, *58*, 2438−2445.
(64) Stein, S. E.; Rabinovitch, B. S. *Chem. Phys. Lett.* **1977**, *49*, 183−188.
(65) Miller, W. H. *J. Chem. Phys.* **1976**, *65*, 2216−2223.
(66) Graul, S. T.; Carpenter, C. J.; Bushnell, J. E.; van Koppen, P. A. M.; Bowers, M. T. *J. Am. Chem. Soc.* **1998**, *120*, 6785−6796.
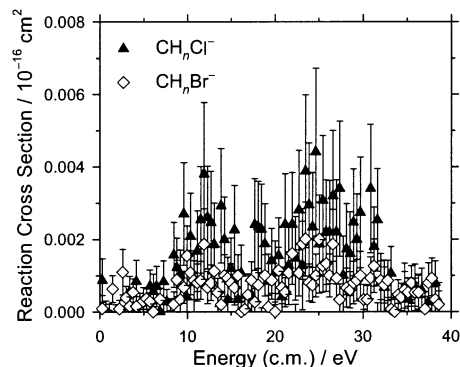
Figure 3. Single-collision cross sections for the product ions Br$^-$ and ClBr$^-$ from the reaction of Cl$^-$ + CH$_3$Br as a function of relative collision energy in the center-of-mass frame. The ion−dipole capture cross section is calculated from the model of Su.[68] Phase space theory cross sections for Br$^-$ and ClBr$^-$ are calculated with the parameters in Table 2 and convoluted over experimental energy distributions.

statistical limit. The PST model is identical to that used for cross sections, except that the harmonic oscillator approximation is used for the densities of states and only the ion-induced dipole potential is used. The contribution of experimental energy broadening to the velocity distributions is calculated by using the Monte Carlo simulation program VELSIM developed by Scott L. Anderson (University of Utah).[67] The simulation includes the Cl$^-$ ion beam energy spread and the CH$_3$Br thermal velocity distribution.

Integral Cross Section Results and Discussion

Survey mass spectra exhibited the major products Br$^-$ and ClBr$^-$ plus CH$_n$Cl$^-$ and CH$_n$Br$^-$ (n = 0, 1, or 2) as very minor channels. No Cl$^-$ (CH$_3$Br) adducts are observed, indicating that all ion−molecule complexes formed in the bimolecular collisions dissociate within the 0.4-ms detection time window. Figure 3 shows the reaction cross sections for the Br$^-$ and ClBr$^-$ channels and Figure 4 shows the cross sections for the CH$_n$Cl$^-$ and CH$_n$Br$^-$ channels. For comparison, we have plotted in Figure 3 the theoretical Cl$^-$ + CH$_3$Br ion−dipole capture-collision cross section from parametrized trajectory calculations.[68] Table 1 lists the experimental enthalpies of reaction for product channels that could influence the cross-section behavior.[69−76]

(67) Chiu, Y.; Fu, H.; Huang, J.; Anderson, S. L. *J. Chem. Phys.* **1995**, *102*, 1199.
(68) Su, T. *J. Chem. Phys.* **1994**, *100*, 4703.
(69) Gurvich, L. V.; Veyts, I. V.; Alcock, C. B. *Thermodynamic Properties of Individual Substances,* 4th ed.; Hemisphere Publishing Corporation: New York, 1989; Vol. 1, Elements O, H (D, T), F, Cl, Br, I, He, Ne, Ar, Kr, Xe, Rn, S, N, P and Their Compounds, Parts 1−2.
(70) Gurvich, L. V.; Veyts, I. V.; Alcock, C. B. *Thermodynamic Properties of Individual Substances,* 4th ed.; Hemisphere: New York, 1991; Vol. 2, Elements C, Si, Ge, Sn, Pb, and Their Compounds, Parts 1−2.
(71) Ingemann, S.; Nibbering N. M. M. *J. Chem. Soc., Perkin Trans. 2* **1985**, *837*, 837−840.
(72) Bartmess, J. E. Negative Ion Energetics Data, In *NIST Chemistry WebBook, NIST Standard Reference Database Number 69*; Mallard, W. G.; Linstrom, P. J., Eds.; National Institute of Standards and Technology: Gaithersburg, MD, July 2001. http://webbook.nist.gov.
(73) Poutsma, J.; Nash, J.; Paulino, J.; Squires, R. *J. Am. Chem. Soc.* **1997**, *119*, 4686−4697.

Figure 4. Cross sections for the product ions CH$_n$Cl$^-$ and CH$_n$Br$^-$, n = 0, 1, or 2, from the reaction of Cl$^-$ + CH$_3$Br as a function of relative collision energy in the center-of-mass frame. Measured at a single cell pressure of 0.03 μbar.
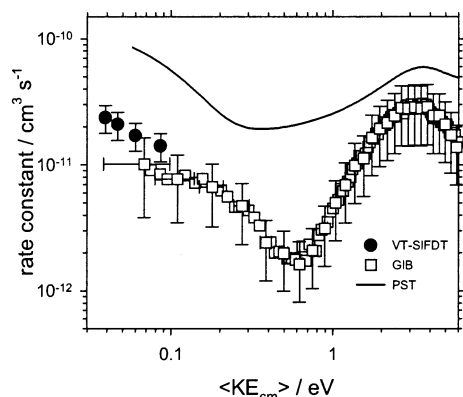
Figure 5. Comparison of the S$_N$2 guided ion beam cross section data with the VT-SIFDT results of Viggiano and co-workers.[34] The circles represent the drift tube rate coefficients as a function of the mean energy in the center-of-mass frame. The squares are the cross sections from the present work converted to rate coefficients as described in the text. The solid line is the phase space theory reaction rate constant calculated with the parameters in Table 2 and convoluted over experimental energy distributions for the GIB experiment.

1. Br$^-$ + CH$_3$Cl Products. The observed cross sections for reaction 2 in Figure 3 compare well with previously reported work at low energies. The experimental cross sections are 0.4% of ion−dipole capture for the energies 0.1−0.2 eV.[68] This compares with previously measured 300 K rate coefficients for reaction 2 of 2.37−2.72 × 10^{-11} cm^3 s^{-1}, giving a reaction efficiency of k_{exp}/k_c = 1%.[9,13,34,68,77] The difference is consistent with the decrease in the cross section with increasing kinetic energy (300 K corresponds to a mean kinetic energy of 0.026 eV). Using a variable-temperature selected-ion flow drift tube (VT-SIFDT), Viggiano and co-workers[34] reported rate constants for reaction 2 as a function of kinetic energy at several temperatures. Their results at 300 K are compared to our reaction cross section data in Figure 5. Our cross sections have been converted to energy-dependent rate coefficients[41] according to $k(\langle E \rangle) = \sigma(E_{cm})v_{rel}$, where $v_{rel} = (2E_{cm}/\mu)^{1/2}$ is the relative collision velocity, $\langle E \rangle = E_{cm} + (3/2)\gamma k_B T$ is the mean energy of the distribution, $\mu = (m_{ion} m_{gas}/(m_{ion} + m_{gas}))$ is the reduced

(74) Hierl, P. M.; Henchman, M. J.; Paulson, J. F. *Int. J. Mass Spectrom. Ion Processes* **1992**, *117*, 475−485.
(75) Born, M.; Nibbering, N. *J. Am. Chem. Soc.* **1994**, *116*, 7210−7217.
(76) Gilles, M.; Ervin, K.; Ho, J.; Lineberger, W. *J. Phys. Chem.* **1992**, *96*, 1130−1141.
(77) Gronert, S.; DePuy, C. H.; Bierbaum, V. M. *J. Am. Chem. Soc.* **1991**, *113*, 4009−4010.
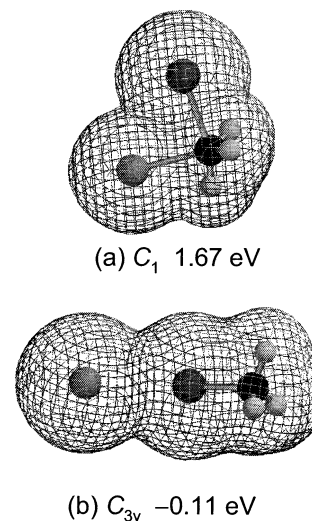
mass, and $\gamma = m_{ion}/(m_{ion} + m_{gas})$. Good agreement is observed between the two experiments where they overlap. In a recent ICR study, Craig and Brauman[78] obtained kinetic energy dependent rate constants for the region 0.04−0.10 eV, also in excellent agreement with the VT-SIFDT results.

a. Low-Energy Behavior. At the lowest collision energy of 0.06 eV, the S_N2 channel exhibits a maximum reaction cross section of 1.3×10^{-16} cm². With increasing collision energies over the range 0.06−0.6 eV, the cross section declines to 0.08 $\times 10^{-16}$ cm². In the low energy region, 0.06−0.2 eV, the reaction and ion−dipole collision cross sections decrease roughly in parallel, but at higher collision energies, 0.2−0.6 eV, the experimental cross section declines more rapidly than the ion−dipole capture cross section. Similar behavior has been previously observed for the F⁻ + CH₃Cl S_N2 reaction[11,17−19] and has been explained by the ion−dipole complex formation partly controlling the reaction at the lowest energies but having less influence at higher collision energies.

Above 0.2 eV, the reaction cross sections decline faster than the ion−dipole capture cross sections. The behavior suggests the S_N2 reaction is transforming from complex-mediated to a direct reaction mechanism (also evident from product velocity distributions, vide infra). The trajectory calculations[18,79,80] have predicted a direct S_N2 reaction mechanism not requiring formation of a complex. As collision energies increase, CH₃Br has less time to orient its dipole to the incoming Cl⁻, resulting in an increased range of encounter angles. Therefore, shorter Cl⁻···CH₃Br interaction times and tighter orientational requirements could explain the rapid decline of the experimental cross sections at collision energies of 0.2−0.6 eV. An orientational effect of this type has been discussed for F⁻ + CH₃Cl by Su et al.[19]

b. High-Energy Feature. Above 0.6 eV, the S_N2 cross section exhibits a rising feature, observed here for the first time. The cross section rises to 0.6×10^{-16} cm² before declining again at energies above 3 eV. This late rising feature is typical behavior for a reaction occurring with an activation barrier and can be attributed a new reaction mechanism. A C_1 transition state for reaction 1 has previously been recognized for front-side attack.[11,81,82] The structure of the C_1 transition state for reaction 2 is shown in Figure 6a. The energy for the front-side transition state at the MP2/aug-cc-pVDZ level is 1.67 eV above reactants, which is much too high to account for the rising cross section originating at 0.6 eV. The new rising feature, therefore, must be due to an increased efficiency of passage over the backside S_N2 central barrier via a new dynamic mechanism. Similar high-energy features were observed for the Cl⁻ + CH₃-Cl → ClCH₃ + Cl⁻ and F⁻ + CH₃Cl → FCH₃ + Cl⁻ reactions.[11,23,24]

Because of the short collision time above 0.6 eV, the reaction mechanism is probably direct with no significant influence from the complex-mediated mechanism. A greater range of reactive collision orientations provides one explanation for the rising cross-section feature. A cut through the PES shown in Figure 7 describes the dependence of the S_N2 barrier height on the Cl−

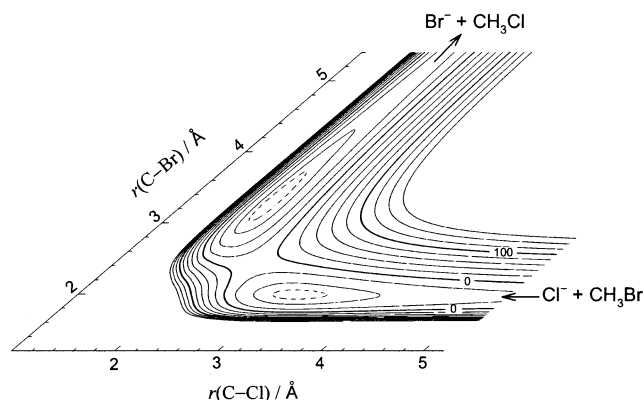(78) Craig, S. L.; Brauman, J. I. *J. Phys. Chem. A* **1997**, *101*, 4745−4752.
(79) Vande Linde, S. R.; Hase, W. L. *J. Chem. Phys.* **1990**, *93*, 7962−7980.
(80) Hase, W. L.; Cho, Y. J. *J. Chem. Phys.* **1993**, *98*, 8626−8639.
(81) Glukhovtsev, M. N.; Pross, A.; Schlegel, H. B.; Bach, R. D.; Radom, L. *J. Am. Chem. Soc.* **1996**, *118*, 11258−11264.
(82) Deng, L.; Branchadell, V.; Ziegler, T. *J. Am. Chem. Soc.* **1994**, *116*, 10645−10656.

(a) C_1 1.67 eV

(b) C_{3v} −0.11 eV

Figure 6. Stationary points found at the MP2/aug-cc-pVDZ level with the total electron density as in Figure 1. (a) The C_1 front-side attack S_N2 transition state and (b) C_{3v} front-side attack bromine abstraction minimum.
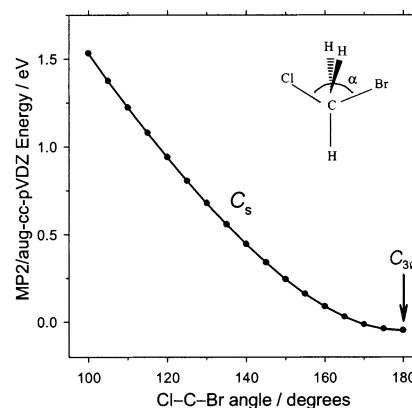
Figure 7. Potential energies of the [Cl−CH₃−Br]⁻ transition state relative to Cl⁻ + CH₃Br as a function of the Cl−C−Br bond angle calculated at the MP2/aug-cc-pVDZ level in C_s symmetry.

C−Br angle. The acceptance cone angles increase from 180 to 135° at 0.5 eV to angles of 180−100° at 1.5 eV. Trajectory calculations by Hase and co-workers[16,79] have indicated a direct reaction can occur with 0.5 eV of energy deposited into the C−Br stretch mode, providing another explanation for the high-energy feature if T→V energy transfer becomes more probable at these collision energies. New trajectory calculations by Wang and Hase[36] also exhibit a dip and recovery in the cross section, although with a minimum at 0.26−0.35 eV versus 0.6 eV observed here. They attribute the feature to a decline in indirect (complex-forming) trajectories and an increase in direct reaction trajectories as the collision energy increases.

The pseudocollinear two-dimensional potential energy surface[52] shown in Figure 8 illustrates the importance of translational to vibrational (T→V) energy transfer for promotion for the S_N2 reaction.[4,83] Initially, the reactants pass along the Cl⁻ + CH₃Br entrance valley at the C−Br equilibrium distance. The translational energy dependence of the reaction can be elucidated by considering the influence of the transition state and the repulsive wall at the top of the entrance valley. At energies of 20 kJ/mol (0.2 eV) and lower (relative to Cl⁻ + CH₃Br) reactants must navigate a tight 'bend' to pass over the transition

(83) Polanyi, J. C. *Acc. Chem. Res.* **1972**, *5*, 161−168.

Figure 8. Contour plot of the potential energy surface of reaction 2 treated as a pseudocollinear pseudotriatomic reaction on mass-skewed coordinates in C_{3v} symmetry. Positions of the H atoms are optimized at the MP2/CEP-121G level with energies calculated at the MP2/aug-cc-pVDZ level. The solid contour intervals are 20 kJ/mol relative to $Cl^- + CH_3Br$ with dashed contours 10 kJ/mol.

state and into the product channel. Reflections off the repulsive wall at the end of the $Cl^- + CH_3Br$ entrance surface send the trajectories back toward reactants and the $Cl^-\cdots CH_3Br$ complex well. For these conditions, T→V energy transfer is not an effective mechanism for the S_N2 reaction. For translational energies above 60 kJ/mol (0.6 eV), the angle of the repulsive wall becomes more favorable for reflecting trajectories toward the $Br^- + CH_3Cl$ product channel. Specular reflections off the repulsive wall and a less restricted opening over the transition state saddle point at higher energies can produce the $Br^- + CH_3Cl$ products in a more efficient direct process. These features of the PES show that for collision energies above 0.6 eV a direct reaction mechanism becomes energetically and dynamically more probable.

The S_N2 cross sections in Figure 3 continue to rise until about 2 eV, where competition from Br abstraction (reaction 3) starts to restrict S_N2. At 3 eV, a collision-induced dissociation (CID) reaction resulting in the products $Br + CH_3 + Cl^-$ is also energetically possible as shown in Table 1. The observed decline in the S_N2 cross sections at energies above 3 eV is, therefore, due to competitive reactions.

c. Phase Space Theory. The experimental results are compared with phase space theory calculations in Figures 3 and 5. PST predicts cross sections or reaction rates that are 4−8 times higher than the GIB experiment at low energies. The magnitude of PST at low kinetic energies depends critically on the height of the central S_N2 energy barrier. The PST model uses the best available ab initio energy from CCSD(T)/431cGTOs calculations[50] (Table 2) with an S_N2 barrier energy of $\Delta E_0^{\ddagger} = -0.095$ eV relative to reactants. This value compares well with a recent kinetic determination of the activation enthalpy using high-pressure mass spectrometry (HPMS),[84] $\Delta H^{\ddagger} = -0.078$ eV, and with other values estimated from kinetic experiments.[9,34,77] We prefer the high level ab initio value, however, because the HPMS kinetics value may be dependent on the experimental temperature and because all of the available "experimental" values of the barrier height are based on fits to statistical rate theory. That leads to a circular argument regarding statistical or nonstatistical behavior. Using the energy of the

(84) Li, C.; Ross, P.; Szulejko, J. E.; McMahon, T. B. *J. Am. Chem. Soc.* **1996**, *118*, 9360−9367.

S_N2 transition state as an adjustable parameter in the PST model to fit our cross sections up to 0.25 eV yields a barrier height of $\Delta E_0^{\ddagger} = -0.02 \pm 0.05$ eV, where the uncertainty allows for a $\pm 50\%$ error in absolute cross sections, a 10% variation in vibrational frequencies, a 5% variation in the rotational constant of the central barrier, varying the energy range of the fit, and the uncertainty of the convolution over the ion energy distribution near the low ion energy cutoff.[41]

At low energies, 0.06−0.6 eV, the PST cross sections exhibit a negative slope similar to the observed energy dependence. As energies increase, the PST cross sections level off to a plateau region followed by a modestly rising feature above 0.9 eV. It is interesting to observe that PST includes a rising feature at higher energies as does experiment. For these energies, there is a faster increase in the densities of states for the tight transition state relative to the orbiting transition state of the reactants because of the lower frequencies of the former. An increase in the accessible densities of states is a complementary explanation to the direct reaction discussed earlier for the increased efficiency of S_N2 above 0.6 eV. However, the experimental cross sections show a deeper dip than predicted by PST, indicating nonstatistical behavior, and as stated above the reaction mechanism is most likely direct at these collision energies. The experimental and PST cross sections decline above 3 eV because of competition from the Br abstraction reaction. PST overestimates the magnitude of the $ClBr^-$ cross sections because of the use of a loose orbiting transition state and because of other dissociative processes at higher energies not included in the PST model.

As a check of the effect of the molecular parameters on the PST calculation, we also used the parameters from the work of Graul and Bowers,[33] who estimated somewhat different frequencies and a central barrier height of $\Delta E_0^{\ddagger} = -0.085$ eV below reactants (versus -0.095 eV from the CCSD(T) calculation[50]). These parameters give cross sections about 40% smaller as compared with the cross sections using the parameters in Table 2, but the energy dependence is identical. The magnitude difference is due in about equal parts to the different barrier height and different vibrational frequencies.

The barrier height in the PST model must be raised from the CCSD(T)[50] value of -0.095 eV up to -0.02 ± 0.05 eV in order to slow the PST reaction probability to match experiment. The ab initio energies for the barrier height have been calculated at a high level of theory and appear to be nearly converged. Therefore, the observation that the experimental cross sections are smaller than the PST predictions is likely due to nonstatistical behavior rather than the barrier being higher than predicted. The inefficiency of the reaction compared with PST corroborates the interpretation of trajectory calculations by Hase and co-workers[4,16,26,28] that the reaction exhibits nonstatistical and non-RRKM dynamical bottlenecks in the entrance channel and at the barrier. However, the effect in terms of cross-section magnitude is relatively small at low energies and this interpretation assumes that the PST model gives the true "statistical" rate.

2. $ClBr^- + CH_3$ Products. For reaction 3, we observe (Figure 3) a small initial feature rising from a threshold energy of $E_0 = 180 \pm 40$ kJ/mol (1.9 ± 0.4 eV), as obtained by an empirical threshold law fit, followed by a more rapid increase beginning at 3 eV and a peak at 6 eV. Cross sections for $ClBr^-$, reaction 3, have previously been published by Cyr et al.[39] for

Table 3. Ab Initio and Experimental Electron Affinities (eV) of Selected Dihalides

	CCSD(T)/ aug-cc-pVTZ	experiment
ClBr	2.47	
Cl$_2$	2.43	2.40 ± 0.20,[a] 2.45 ± 0.15,[b] 2.32 ± 0.10,[c] 2.38 ± 0.10[d]
Br$_2$	2.51	2.64 ± 0.20,[a] 2.55 ± 0.10,[b] 2.62 ± 0.20,[c] 2.51 ± 0.10[d]

[a] Neutral beam ionization, Dispert and Lacmann.[86] [b] Neutral beam ionization, Baede.[85] [c] Endoergic electron transfer, Lifshitz et al.[87] [d] Enodergic electron transfer, Chupka et al.[88]

seven collision energies in the range 2−15 eV. Their ClBr$^-$ cross sections exhibit an onset energy of about 2 eV and a maximum at 7 eV and are in reasonable agreement with the ClBr$^-$ cross sections presented here.

The measured threshold energy is near the thermochemical endothermicity of reaction of $\Delta_3 H_0 = 184 \pm 14$ kJ/mol, estimated from established enthalpies of formation[69,70] and a theoretical electron affinity calculated here at the CCSD(T)/ aug-cc-pVTZ level, EA(ClBr) = 2.47 ± 0.13 eV. The error bars for EA(ClBr) are estimated by comparing the CCSD(T)/ aug-cc-pVTZ values for the EA(Br$_2$) = 2.51 eV and EA(Cl$_2$) = 2.43 eV with experimental values shown in Table 3.[85−88] Good agreement between the threshold energy and theoretical values supports the accuracy of EA(ClBr) = 2.47 ± 0.13 eV from the CCSD(T) calculation.

At about 3 eV, the ClBr$^-$ cross sections exhibit a second stronger rising feature increasing to 1.0×10^{-16} cm^2 by 6.0 eV. The 3 eV onset energy is coincident with a decreasing S$_N$2 cross section and the energy where the CID reaction to form Cl$^-$ + CH$_3$Br → CH$_3$ + Br + Cl$^-$ may proceed. Cross sections for the CID reaction are not measured because the Cl$^-$ product is indistinguishable from the Cl$^-$ reactant ion by mass. The ClBr$^-$ cross sections appear to be enhanced at the energies where the CID reaction can proceed. This behavior has been previously recognized[11,25] and might be explained by the association of the two halide species from an impulsive dissociative process resulting in the dihalide ion. Above 6.0 eV, the ClBr$^-$ cross sections decline because of further dissociation of ClBr$^-$ to Cl$^-$ + Br.

Similar cross section behavior was previously observed for FCl$^-$ formation from the reaction F$^-$ + CH$_3$Cl.[11] In the previous work a minimum structure was located on the PES for the front-side halide abstraction reaction. A minimum structure for the front-side attack mechanism for reaction 3 is also found here, calculated at MP2/aug-cc-pVDZ level, and is shown in Figure 6b. However, this minimum is shallow (−0.11 eV relative to Cl$^-$ + CH$_3$Br) and might not be important for a direct abstraction reaction at elevated energies. At the energies of reaction 3, the C_1 front-side transition state region of the PES, Figure 6a, can also be accessed.

3. Dissociative and Detachment Channels. The CH$_n$Cl$^-$ and CH$_n$Br$^-$ cross sections (Figure 4) are near the detection limit and were measured at a single pressure with low resolution to maximize sensitivity. Determination of the exact masses of these species was impractical because the weak signals fall below

the detection limit as the mass resolution of the quadrupole mass spectrometer is increased. Table 1 shows that many dissociative product channels are accessible at high energies. Below 5 eV, the only accessible products are CH$_2$Br$^-$ + HCl and CH$_2$Cl$^-$ + HBr. At higher energies, formation of CHCl$^-$ becomes possible above 5 eV, along with CH$_2$Cl$^-$, CHCl$^-$, CH$_2$Br$^-$, CBr$^-$ and CCl$^-$ above 6 eV (Table 1). The cross sections are greatest above 10 eV, suggesting the main products are dissociative channels.

In ion beam/gas cell experiments on Cl$^-$ + CH$_3$Br, White et al.[89] reported that electron detachment cross sections, Cl + e$^-$ + [CH$_3$Br], rise from an apparent threshold at 6 eV (well above the thermodynamic detachment threshold of EA(Cl)[72] = 3.6 eV) to a plateau of 10 × 10^{-16} cm^2 above 100 eV (c.m.). That indicates that the electron detachment process is an additional competitive channel leading to the decline of reactions 2 and 3 above 6 eV. White et al.[89] further reported strong inelastic scattering of Cl$^-$ at these higher energies, which they attributed to processes resulting in dissociation of CH$_3$Br.

Product Velocity Distribution Results and Discussion

1. Br$^-$ + CH$_3$Cl Products. The relative axial velocity distributions for the S$_N$2 products at a series of collision energies are shown in Figure 9. For isotropic scattering, the axial velocity distributions peak at zero velocity in the center-of-mass frame because side-scattered ions (90° deflection angle) have zero velocity component along the beam direction for all azimuthal angles 0−2π. Scattering is described as "forward" when the product that contains the chlorine atom is scattered in the direction of the reactant Cl$^-$ ion velocity vector. That is, the measured Br$^-$ velocities have been converted into relative c.m. velocities according to eq 9 with a change of sign to represent scattering of neutral CH$_3$Cl. At the lowest collision energy of 0.10 eV, the S$_N$2 product velocity distribution is symmetric with respect to the c.m. velocity, which is consistent with complex formation and isotropic scattering. The peaks of the velocity distributions move toward forward scattering at collision energies from 0.2 to 0.5 eV, then a new backscattered peak grows in at 0.5 eV and higher. These asymmetric distributions are experimental proof of direct reaction mechanisms.

Figure 9 shows that most of the product velocities fall into the range where the detected Br$^-$ ions have forward velocity in the laboratory frame. However, a fraction of the Br$^-$ ions could be backscattered in the lab and lost. Judging by the peak velocities and shapes of the velocity distributions, the impact of backward scattered ions on the integral cross section measurements is less than 15% below 1 eV and negligible at higher collision energies.

The product velocity distributions from phase space theory are displayed in Figure 9. The PST velocity distributions are less sensitive to molecular parameters than are the PST reaction rates, and they vary fairly slowly with collision energy. Little difference is found between our molecular parameters (Table 2) and those used by Graul and Bowers.[32,33] Also shown in Figure 9 at 0.10 eV is the contribution of experimental energy broadening to the PST model. The broadening effects on product velocity distributions are minor.

a. Lowest Collision Energy, 0.10 eV. The velocity distribution of S$_N$2 at the collision energy of 0.10 eV is symmetric and

(85) Baede, A. P. M. *Physica* **1972**, *59*, 541−544.
(86) Dispert, H.; Lacmann, K. *Chem. Phys. Lett.* **1977**, *47*, 533−536.
(87) Hughes, B. M.; Lifshitz, C.; Tiernan, T. O. *J. Chem. Phys.* **1973**, *59*, 3162−3181.
(88) Chupka, W. A.; Berkowitz, J.; Gutman, D. *J. Chem. Phys.* **1971**, *55*, 2724−2733.

(89) White, N. R.; Scott, D.; Huq, M. S.; Doverspike, L. D.; Champion, R. L. *J. Chem. Phys.* **1984**, *80*, 1108−1115.

agrees well with the prediction of the PST model. The symmetric, statistical scattering at 0.10 eV indicates that the S$_N$2 reaction is complex-mediated at the lowest collision energies.

The trajectory calculations of Hase and co-workers[4,26−28] show nonstatistical dynamic bottlenecks in the energy transfer from the inter- to the intramolecular modes of CH$_3$Br. At a collision energy of 0.10 eV, Figure 9 shows that the velocity distributions are nevertheless statistical according to the PST model. That is not necessarily inconsistent with the reported nonstatistical effects in the entrance channel, because the product energy distribution reflect the dynamics of reactive trajectories that have made it through the bottlenecks to the complex and over the barrier. That is, the product energy distribution can be statistical even if the overall bimolecular reaction is not statistical. For example, a trajectory study[90] shows that strong coupling in the exit channel can lead to statistical product energies even when the unimolecular lifetime is non-RRKM.

The statistical behavior observed for S$_N$2 velocity distributions at 0.10 eV can be compared with previous work on metastable Cl$^-$···CH$_3$Br complex dissociation by Graul and Bowers,[32,33] who reported kinetic energy release distributions for the products Br$^-$ + CH$_3$Cl. They observed significantly narrower kinetic energy release distributions experimentally than predicted by PST, implying higher internal excitation of CH$_3$Cl. Although that result is different than observed here at 0.10-eV c.m., the experimental conditions are also significantly different. For the metastable ion dissociation experiment, the Cl$^-$···CH$_3$Br adducts are formed by association reactions in the ion source between Cl$^-$ ions and CH$_3$Br at a pressure of 0.05−0.1 Torr. Only at these relatively high source pressures were the metastable Cl$^-$···CH$_3$Br ions detected in the experiment, which requires Cl$^-$···CH$_3$Br lifetimes of 10−20 μs before dissociation.[32,33] Collisions in the ion source significantly cool the internal energy and angular momentum distributions of the metastable Cl$^-$··· CH$_3$Br complexes, but this initial ion internal energy distribution is poorly characterized. No matter what the source ion energy distribution, however, the subsequent metastable ion dissociation preferentially samples complexes with energies below reactants and just above the central barrier, i.e., below 0 eV and probably closer to −0.095 eV. In contrast, the present experiments sample all of the angular momenta from random impact parameters in a single bimolecular collision, at a mean total energy of 0.15 eV for the nominal collision energy of 0.10 eV (including the mean energy of the kinetic energy distribution[41] and the CH$_3$-Cl internal energies at 300 K). The contrast between the statistical product energy distribution in the bimolecular reaction here and the significantly nonstatistical behavior found in the metastable ion study may be attributed, therefore, to different distributions of internal energy and angular momentum.

Hase and co-workers[15,16] have also used trajectory calculations to investigate energy disposal into products on three different potential energy surfaces. Striking differences were found in the detailed dynamics obtained from the three surfaces. One PES gives a cold relative translational energy distribution in agreement with the Graul and Bowers experiment. The other two surfaces yield product translational energy distributions similar to and a factor of 3 more energetic than the PST statistical prediction, respectively. Hase and co-workers[16]

(90) Hase, W. L. *Chem. Phys. Lett.* **1979**, *67*, 263−266.
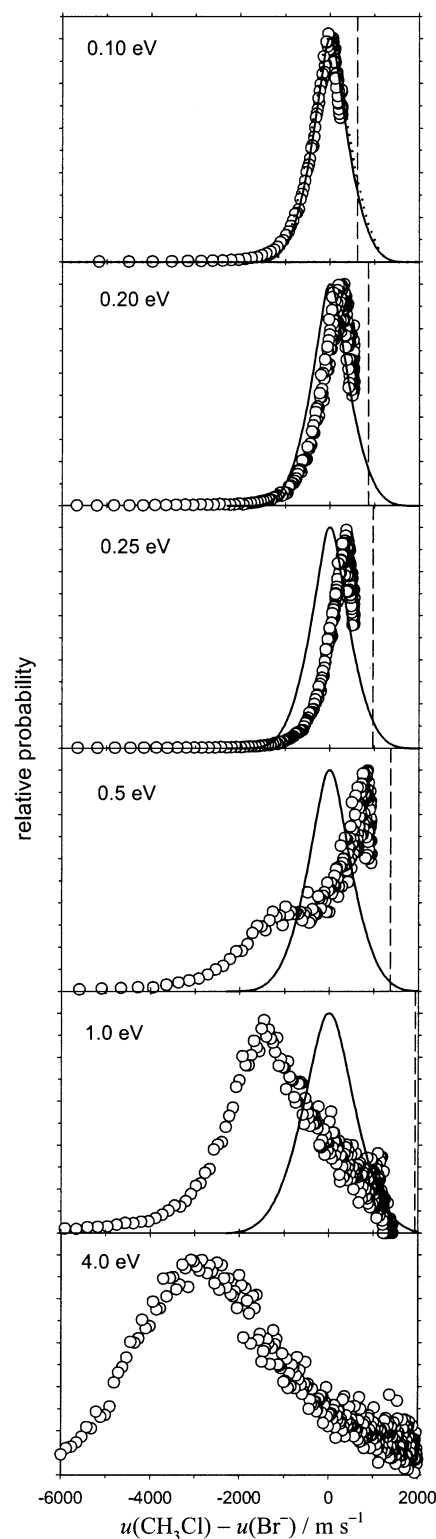
Figure 9. Relative axial velocity distributions for the products of reaction 2 at 0.10, 0.20, 0.25, 0.5, 1.0, and 4.0 eV. Circles are the experimental results with the solid line showing the phase space theory velocity distributions, which peak at zero c.m. velocity. The PST model convoluted over experimental energy distributions is shown by the dotted line at 0.10 eV. Positive values of the axial relative velocities correspond to forward scattering of the CH$_3$Cl product relative to the Cl$^-$ velocity vector. The dashed vertical lines are the relative velocities above which the Br$^-$ ions would be backward scattered in the lab frame.

concluded that trajectories on a higher-level ab initio potential energy surface would be required to elucidate all aspects of the

kinetics and dynamics. For comparison with experiments, dynamics calculations also need to take into account the different energy and angular momentum distributions and the kinetic time windows of various experiments. The total energy used for the classical trajectory calculations on $Cl^-(CH_3Br)$ complex decomposition[16] was 11.3 kJ/mol or 0.12 eV above reactants, similar to the mean total energy of the guided beam experiment at 0.10-eV c.m. collision energy, but significantly higher than the energies sampled in the metastable ion dissociation experiment of Graul and Bowers.[32,33]

Viggiano and co-workers[34] observed that at fixed kinetic energy the rate constants for reaction 2 remain unchanged when the CH_3Br temperature is varied from 207 to 564 K, while the rates decline for a comparable increase in kinetic energy. That is in contradiction of statistical behavior as modeled by RRKM theory,[35] which shows higher rate constants with increasing internal temperature (although the RRKM model[35] did not consider the effect of the experimental kinetic energy distributions). We cannot directly compare the temperature-dependent rate coefficients with our energy-dependent cross sections or product velocity distributions because the CH_3Br temperature cannot be separately controlled with the current experimental apparatus. Our product velocity distributions are sensitive to a different part of the dynamics than are the rate coefficients versus reactant internal energies in the work of Viggiano and co-workers.[34]

b. Higher Collision Energies. With just a small increase of collision energy to 0.20 and 0.25 eV, the velocity distributions become decidedly asymmetric with a preference for forward scattering of the CH_3Cl product, as exhibited in Figure 9. Forward scattering implies that the reaction is not statistical, for which the complex would dissociate isotropically. Asymmetric scattering results from an interaction between the reactants on a time scale less than a rotational period of the complex (about 10^{-12} s). Asymmetric scattering confirms that the reaction mechanism is changing from the complex-mediated to a more direct mechanism. This behavior is consistent with the more rapidly decreasing cross sections over the range 0.2–0.6 eV.

The velocity distribution at 0.5 eV in Figure 9 shows that there are two independent mechanisms with the forward-scattered peak now centered around 750 m s^{-1} and a new weaker backscattered peak at -1000 m s^{-1}. The backscattering feature becomes dominant at 1.0 and 4.0 eV. Backward scattering of CH_3Cl is consistent with a direct rebound mechanism. This new behavior cannot be explained by front-side attack because the energy is below that of the C_1 transition state (Figure 6), at least near the threshold of the feature. Instead, it is most likely due to a combination of a new efficient direct, impulsive backside attack mechanism and angular momentum constraints at higher kinetic energies that favor collisions with low-impact parameters.

At a collision energy of 4.0 eV, the CH_3Cl velocity distribution peaks at about -3000 m s^{-1}. Converting the peak velocity into a kinetic energy release for reaction 2 gives 1.4 eV. The available energy for products is approximately 4.4 eV, which means about 3.0 eV remains in the internal degrees of freedom of CH_3Cl, on average. Such high internal excitation is close to the dissociation limit of CH_3Cl, which supports the conclusion that the decline in the total cross section for reaction 2 above 4
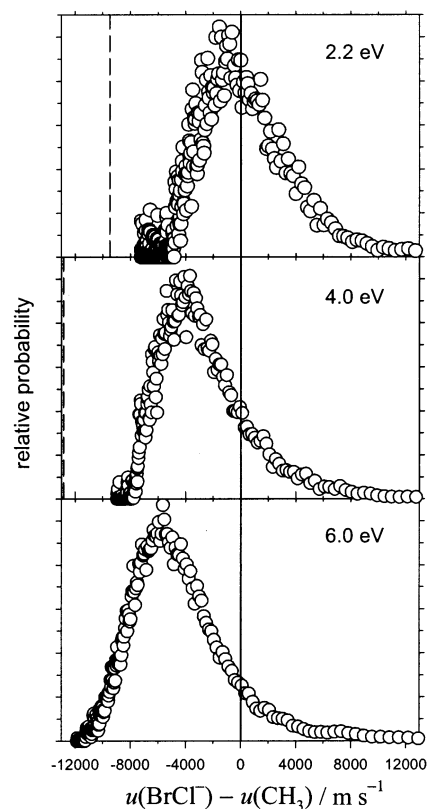
Figure 10. Relative axial velocity distributions for the products of reaction 3 at 2.2, 4.0, and 6.0 eV. Positive values of the relative axial velocities correspond to forward scattering of the $ClBr^-$ product relative to the Cl^- velocity vector. The solid vertical line is the zero center-of-mass velocity; the dashed vertical lines are the relative velocities below which the $ClBr^-$ ions would be backward scattered in the lab frame.

eV is due to competitive dissociation channels. The high internal excitation of CH_3Cl also absorbs energy that might otherwise cause collisional electron detachment, which was observed[89] only above 6 eV.

2. $ClBr^-$ + CH_3 Products. Velocity distributions for the Br abstraction reaction at a series of collision energies are shown in Figure 10. At 2.2 eV, just above the threshold, the $ClBr^-$ product exhibits nearly symmetrical scattering around the zero center-of-mass velocity. The symmetric scattering may also indicate a relatively long interaction between the reactants or products as they pass along the PES. Halogen abstraction has previously[11,25] been identified to proceed via a steep exit surface, indicating that the important interaction is between the products as they surmount the exit barrier. Figure 10 shows asymmetric, strongly backscattered velocity distributions for $ClBr^-$ at collision energies of 4 and 6 eV, corresponding to the second rising feature of the $ClBr^-$ cross section (Figure 3). The observed backscattering indicates that a direct rebound mechanism is responsible for this feature. This behavior is consistent with the impulsive rupture model discussed earlier where T → V energy transfer results in CH_3–Br dissociation, and an association of the halide species to form $ClBr^-$ is responsible for the cross sections at energies above 3 eV. A direct rebound mechanism is also exhibited by S_N2 at energies above 0.6 eV. Br abstraction likely results from front-side attack while S_N2 proceeds via backside attack. Competition between these two direct mechanisms explains the decrease in the Br^- cross section above 3 eV.

The peak scattering of ClBr$^-$ velocities at 6.0 eV can be used to estimate a relative kinetic energy release for reaction 3 of approximately 2.5 eV. The total energy available for the products is approximately 4.3 eV, giving internal excitation of 1.8 eV for ClBr$^-$ + CH$_3$. The available energy is more evenly distributed in the direct front-side mechanism of reaction 3 than in the direct backside mechanism of reaction 2. Direct S$_N$2 backside attack enforces the inversion of the methyl group, whereas front-side attack results in the rearrangement from a tetrahedral CH$_3$Br to planar geometry of CH$_3$. The energy deposited into internal energy for reaction 3 can account for the dissociation of ClBr$^-$, for which D_0(ClBr$^-$) = 1.3 eV. The dissociation of ClBr$^-$ → Cl$^-$ + Br explains the decline of the ClBr$^-$ cross section observed in Figure 3 for collision energies above 6 eV.

Statistical and Nonstatistical Behavior in the Cl$^-$ + CH$_3$Br S$_N$2 Reaction

On the whole, the present results demonstrate strongly nonstatistical behavior for reaction 2. Except at the lowest collision energy, the product velocity distributions exhibit asymmetric forward or backward scattering, proving that the reaction mechanisms are direct and definitely nonstatistical. Below 0.2 eV, the reaction cross sections are smaller by a factor of 4−8 than predicted by phase space theory, in qualitative agreement with classical trajectory calculations[4,15,16,28] that show dynamic bottlenecks for formation of the entrance-channel complex, nonstatistical energy transfer within the complex, and non-RRKM recrossings of the central barrier.

The S$_N$2 product velocity distribution at the lowest measured collision energy (0.1 eV) is the single experimental observation in the present work that implies statistical behavior. The velocity distribution is symmetric about the center-of-mass and agrees with the prediction of phase space theory as shown in the top panel of Figure 9. Although we cannot measure product distributions down to room-temperature kinetic energies (0.026 eV), it would be surprising if the product distributions become asymmetric again at lower energies for single bimolecular collisions. Thus, it appears that statistical behavior is likely for the product energy distributions for the thermal bimolecular S$_N$2 reaction, regardless of nonstatistical behavior of other aspects of the reaction. Once the system achieves its way through suspected dynamic bottlenecks to the central barrier, the degrees of freedom for products are randomized.

In contrast, Graul and Bowers[32,33] observed nonstatistical product energy distributions from metastable dissociation of Cl$^-$···CH$_3$Br complexes, with excess vibrational excitation of the CH$_3$Cl products compared with the phase space theory prediction. The difference between those experiments and the present work on the bimolecular reaction can be explained by the different energy and angular momentum distributions in the two experiments. The long-lived metastable ions have energies below those of a nascent bimolecular collision and just above the central barrier (−0.095 eV relative to reactants). Referring to the pseudocollinear potential energy surface in Figure 8, we can speculate on a dynamic explanation for high vibrational excitation of the metastable dissociation products. The required long metastable ion lifetime (10−20 μs) kinetically selects complexes that are trapped in the entrance well with barely high enough energy (and low enough angular momentum) to pass

over the S$_N$2 barrier. Trajectories at those energies must pass over the saddle point closely parallel to the reaction coordinate, which is a vector pointing toward the product channel but with a large fractional component of CH$_3$−Cl vibrational motion. Assuming a straight trajectory from the saddle point and using geometric considerations in the mass-weighted coordinate system[22] of the PES in Figure 8, one can estimate that about 88% of the available product energy would initially appear as vibrational energy.[91] With a reaction exoergicity of −0.32 eV and an initial total energy of −0.095 eV, that corresponds to 0.20 eV in vibrational energy, in good agreement with the 0.17 eV of "fixed" vibrational energy reported by Graul and Bowers.[33]

At the higher collision energy accessed in the present experiments (about 0.1 eV or 10 kJ/mol), reactive trajectories can pass over the barrier with a wider range of energy in degrees of freedom perpendicular to the reaction coordinate and at geometries farther away from the saddle point. Reactive trajectories can include those that have passed through more than one turning point in the entrance channel, either in the complex region or bouncing off the inner repulsive wall. These effects will tend to randomize the energy distributions as the system passes over the barrier region and through the exit channel, leading to statistical behavior as regards product velocities. At still higher energies, trajectories can reflect off the repulsive wall and pass directly to the S$_N$2 product channel without complex formation, accounting for the observed asymmetric product energy distributions.

Despite the observed statistical product energy distribution at low collision energy, the magnitude of the cross section of reaction 2 is 4−8 times lower than predicted by phase space theory and 250 times lower than the ion−dipole capture cross section. It is useful to elucidate the reasons for the low reaction efficiency. In the PST model, the ion−molecule complex is formed at the collision-capture rate on the long-range electrostatic potential. The most important factors in PST favoring back-dissociation to reactants over the formation of S$_N$2 products are (1) the relative densities of states of the two decomposition channels and (2) angular momentum constraints.[35] Figure 11 shows the calculated rovibrational sums of states of the two channels as a function of energy. The sums of states of the loose transition state for the Cl$^-$ + CH$_3$Br entrance channel quickly overtake those of the tight S$_N$2 transition state, favoring the back-decomposition to reactants by a 13:1 at a total energy of 0.15 eV above the Cl$^-$ + CH$_3$Br reactants.[92] Thus, the low density of states of the tight transition state at the central barrier disfavors decomposition of the complex to S$_N$2 products. However, the calculated factor of 13 is far smaller than the observed factor of 250 compared with the ion−dipole capture model. Therefore, the densities of states only partly explain the observed low reaction efficiency.

The effect of the orbital angular momentum on reaction 2 is illustrated in Figure 12a. This shows a calculated C_{3v} collinear

(91) Based upon the velocity vector tangent to the reaction coordinate at the barrier forming a 70° angle with the C−Br translational coordinate. Because this simple model assumes no energy transfer between vibration and translation in the exit channel, it is probably an upper limit.

(92) At higher energies, beyond those shown in Figure 11, the preference for the back-reaction declines to a minimum of 2:1 at 8 eV. The sum of states for the S$_N$2 transition state below the energy of reactants is extremely small (<300), suggesting that quantum effects could be important for the metastable ions observed at those energies by Graul and Bowers.[32,33]
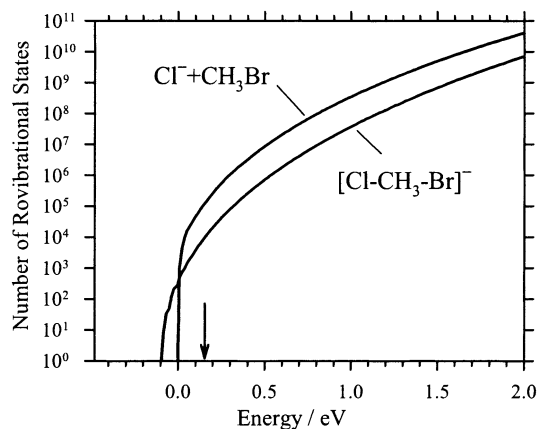
Figure 11. Rovibrational sums of states for the Cl^- + CH_3Br reactants (loose transition state) and the $[Cl\cdot\cdot CH_3\cdot\cdot Br]^-$ S_N2 central barrier (tight transition state) calculated from the molecular parameters in Table 2 using Beyer–Swinehart Stein–Rabinovitch direct counting, as a function of the energy above Cl^- + CH_3Br. The arrow marks the mean total energy (translational and internal energy) of 0.15 eV that pertains to the nominal collision energy of 0.10 eV c.m. in the present experiments.

potential energy curve at the MP2/aug-cc-pVDZ level, with the effective centrifugal potential added in for several values of the orbital angular momentum. Details of this treatment have been given previously.[25] Figure 12a illustrates that the effective potential at the S_N2 transition state is far more important in limiting the reaction than is the centrifugal barrier in the entrance channel. A simple collision model described previously[25] can be used to predict the maximum reaction cross section for overcoming the effective potential barrier as a function of collision energy. This model is shown in Figure 12b. The angular momentum barrier reduces the cross sections by about an order of magnitude from the ion–dipole capture cross section at 0.1 eV. Figure 12b shows that the energy dependence of the PST cross sections largely follows the trend for crossing the central angular momentum barrier, illustrating the importance of the conservation of orbital angular momentum generated by the collision.[93]

Thus, the inefficiency of the S_N2 reaction as predicted by PST is a combination of the low density of states and the high angular momentum barrier at the central S_N2 transition state. The details of explicit conservation of total angular momentum (orbital and rotational) also play a role in the PST model. The remaining deviation between the PST model and experiment can then be attributed to "nonstatistical" effects, assuming that the PST model accurately represents the statistical limit. Because of approximations in the PST model and because the PST and RRKM approaches give different rate constants,[15,92] that assumption is not necessarily reliable at low energies where the primary deviation from experiment is the magnitude of the cross sections. However, the observed energy dependence of the cross sections and the product velocity distributions at higher energies (>0.2 eV) are clearly different than the statistical prediction.

---

(93) For calculating the central barrier collision model cross section, we used a moment of inertia at the barrier corresponding to the approximate spherical rotational constant used in the phase space theory model, $B_s = (ABC)^{1/3} = 0.16$ cm^{-1} from $A = 4.85$ cm^{-1} and $B = C = 0.030$ cm^{-1} (Table 2). The magnitude of the effective potential depends strongly on this rotational constant. Because the $[Cl-CH_3-Br]^-$ transition state is highly nonspherical and because the angular momentum barrier is especially important for this reaction, explicit consideration of the transition state as a symmetric rotor could affect the PST reaction probabilities, even though as a general rule the spherical rotor approximation has been found to be accurate.[15,55,56]
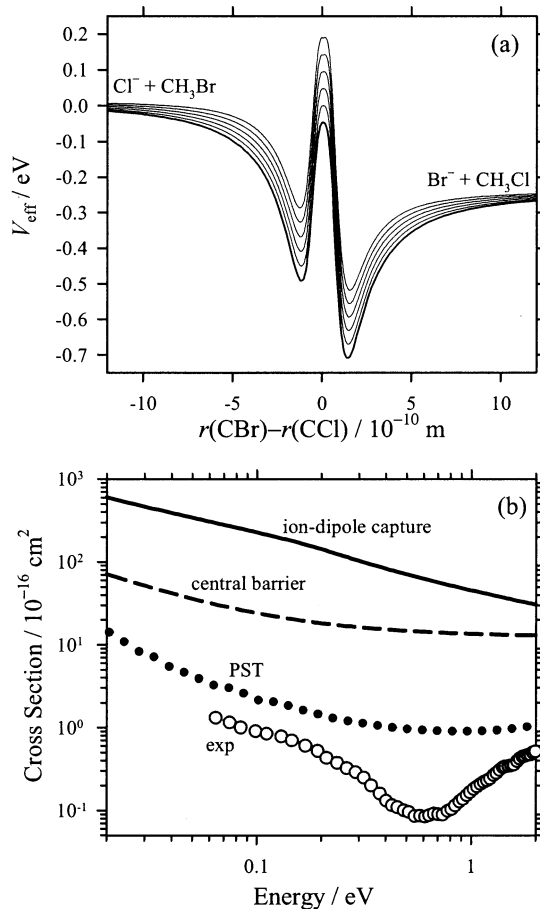
Figure 12. (a) Effective potential energy curves for reaction 2. The lowest curve is the potential energy calculated at the MP2/aug-cc-pVDZ level. The higher curves are the effective potential energies for increasing amounts of orbital angular momentum,[25] $Eb^2 = 100, 200, 300, 400, 500$ kJ mol^{-1} Å^2 or $L^2 \approx 8, 16, 24, 33, 41$. (b) Comparison of model cross sections. Collision-capture cross section for Cl^- + CH_3Br calculated for the ion–dipole potential using the parametrized trajectory calculations of Su[68] (solid line). Cross section for crossing the angular momentum barrier at the S_N2 central barrier (dashed line). Phase space theory model (solid dots). Experimental cross sections from the present work (open circles). The model cross sections do not include convolutions over internal or kinetic energy distributions.

Summary

The bimolecular nucleophilic substitution (S_N2) reaction Cl^- + $CH_3Br \rightarrow CH_3Cl$ + Br^- displays five distinctive patterns of behavior for the collision energies of 0.06–24 eV.

(1) For low collision energies from 0.06 to 0.2 eV, the S_N2 reaction cross sections exhibit lower reaction efficiency than the ion–dipole collision cross section or than predicted statistically. The low efficiency of the reaction can be attributed to the low density of states and high angular momentum barrier at the central S_N2 transition state, with possible additional inefficiency due to nonstatistical dynamic bottlenecks for reaching the S_N2 central barrier as predicted by trajectory calculations.[4,15,16] The velocity distribution of symmetrically scattered CH_3Cl + Br^- products at 0.10 eV agrees with an isotropic statistical distribution predicted by PST, implying statistical behavior in the exit channel for the bimolecular reaction at near-thermal energies.

(2) At collision energies of 0.2–0.6 eV, the S_N2 reaction cross sections decrease with a greater slope than ion–dipole capture or phase space theory and have asymmetric product velocity

distributions with CH$_3$Cl forward scattering, showing that energy disposal is definitely nonstatistical. The reaction proceeds through an intermediate with a lifetime less than a rotational period of the complex and changes from the complex-mediated to a more direct reaction mechanism.

(3) At 0.6−3.0 eV the cross sections for reaction 2 exhibit a new rising feature and the velocity distributions show that CH$_3$-Cl is backward scattered. The behavior is explained by a new direct rebound reaction mechanism but still with backside attack at least near the threshold of this feature. The increasing efficiency can be explained by the opening up of the orientational cone of acceptance and reflections off the inner repulsive wall more favorably directing trajectories toward the product channel at higher energies.

(4) At energies above 3.0 eV, the S$_N$2 cross section declines due to competition from the Cl$^-$ + CH$_3$Br → CH$_3$ + ClBr$^-$ reaction. The Br abstraction reaction rises from its thermodynamical threshold at 1.9 ± 0.4 eV. A small initial rise in the cross sections are accompanied by a velocity distribution exhibiting close to symmetrical scattering. A second stronger rise in the ClBr$^-$ cross sections is observed at energies above 3.0 eV with the velocity distributions now showing a backward scattering. The direct rebound behavior is consistent with an impulsive front-side attack competing with the direct backside attack of S$_N$2.

(5) At higher energies, both the S$_N$2 and bromine abstraction cross sections decline because of dissociative channels producing Cl$^-$ or collisional electron detachment.

The product velocity distributions measured in this work have uncovered several different reaction mechanisms for reactions 2 and 3 in various energy regimes, adding to previous experimental information about this system. Great insight into the mechanism of reaction 2 has also been provided by theory, including classical trajectories[4,15,16,36] and quantum dynamics calculations.[12,20,21,28] However, because of uncertainties in the potential energy surface, issues with treatment of zero-point vibrational energy for classical trajectories, and limits on the number of degrees of freedom that can be treated in quantum calculations, quantitative theoretical descriptions of this system remain a challenge.

JA021003+